npj | Quantum Materials

www.nature.com/npjquantmats

ARTICLE OPEN

Magic-angle semimetals

Yixing Fu[1,5], Elio J. König[1,5], Justin H. Wilson[1,2,5], Yang-Zhi Chou[3,4] and Jedediah H. Pixley[1]✉

Breakthroughs in two-dimensional van der Waals heterostructures have revealed that twisting creates a moiré pattern that quenches the kinetic energy of electrons, allowing for exotic many-body states. We show that cold atomic, trapped ion, and metamaterial systems can emulate the effects of a twist in many models from one to three dimensions. Further, we demonstrate at larger angles (and argue at smaller angles) that by considering incommensurate effects, the magic-angle effect becomes a single-particle quantum phase transition (including in a model for twisted bilayer graphene in the chiral limit). We call these models "magic-angle semimetals". Each contains nodes in the band structure and an incommensurate modulation. At magic-angle criticality, we report a nonanalytic density of states, flat bands, multifractal wave functions that Anderson delocalize in momentum space, and an essentially divergent effective interaction scale. As a particular example, we discuss how to observe this effect in an ultracold Fermi gas.

npj Quantum Materials (2020)5:71 ; https://doi.org/10.1038/s41535-020-00271-9

INTRODUCTION

The engineering of band structures with non-trivial topological wave functions has achieved success in creating and controlling quantum phases in a variety of systems such as doped semiconductors[1–4], ultracold atoms[5,6], and metamaterials[7,8]. With the recent advance in twisted graphene heterostructores[9–12] (i.e., "twistronics") new, strongly interacting, solid state systems can now also be engineered with a rather weakly correlated two-dimensional semimetal (graphene)[13–15]. In these systems, as a consequence of the quenched kinetic energy, correlations dominate the physics and exotic many-body states may form. This interpretation relies on the reduction of the electronic velocity and large increase of the density of states (DOS) which was shown in twisted bilayer graphene (TBG) theoretically[16–19] and experimentally[20–22] prior to the recent groundbreaking discoveries in refs. [9–11]. Understanding the essential single-particle ingredients necessary to build emulators of TBG can help shed light on the strong coupling regime where consensus about the form of an effective low-energy description remains elusive[23–29].

In this manuscript, we develop the theory for twistronic emulators by first distilling the basic physical phenomena that create correlated flat bands out of two-dimensional Dirac cones. Generically, quasiperiodicity that respects the symmetry protecting the Dirac nodes creates flat bands in nodal, semimetallic band structures in a universal fashion near a previously unnoticed single-particle quantum phase transition (QPT)—what we call the "magic-angle" in analogy to TBG. At small angles in TBG, a single-scattering wavevector accounts for the majority of the band flattening[17,30] but misses any QPT. With quasiperiodicity, an infinite sequence of higher wavevectors (i.e., Brillouin zone downfoldings) further flatten the bands and culminate into a QPT. This band flattening occurs irrespective of the topology present, and in fact, many of the models we study have topology distinct from TBG[24]. We demonstrate strong correlations by computing Wannier states within this series of bands; these lead to a Hubbard model with a quenched kinetic energy and relative to this, the interaction scale is increased dramatically. We therefore argue that the single-particle quantum critical state is unstable toward the inclusion of interactions, which form a correlated insulator at half filling.

Crucially, our findings are independent of many of the system's details and, therefore, demonstrate the existence of a wide multitude of engineered, strongly coupled quantum systems that we call magic-angle semimetals. To demonstrate this, we classify the family of these models with symmetry protected nodes (including chiral TBG at moderate twist angles) as well as introduce and solve a series of models; most of which can be straightforwardly realized with existing ultracold atom, trapped ion, and metamaterial experimental setups. Thus, we propose a simple route to emulate the phenomena of magic-angle TBG in a wide variety of quantum many body systems[15,31]. Last, we show that the magic-angle effect can be observed at experimentally relevant time scales and temperatures in interacting ultracold Fermi gases through measurements of wave packet dynamics.

RESULTS

"Magic-angle semimetals"

The whole class of magic-angle semimetal models are governed by Hamiltonians of the form:

$$\hat{H} = \hat{T} + \hat{V} + \hat{U}, \tag{1}$$

containing single-particle hopping $\hat{T}$, a quasiperiodic modulation $\hat{V}$ (such as potential scattering or interlayer tunneling), and interparticle interactions $\hat{U}$. The kinetic term $\hat{T}$ has isolated nodal points in the Brillouin zone where the DOS vanishes in a power law fashion (i.e., semimetallic). The quasiperiodicity in $\hat{V}$ is encoded in an angle originating either from twisted bilayers or the projective construction of quasicrystals[32], and it is characterized by an amplitude W and an incommensurate modulation Q (or twist angle θ).

[1]Department of Physics and Astronomy, Center for Materials Theory, Rutgers University, Piscataway, NJ 08854, USA. [2]Institute of Quantum Information and Matter and Department of Physics, California Institute of Technology, Pasadena, CA 91125, USA. [3]Condensed Matter Theory Center and The Joint Quantum Institute, Department of Physics, University of Maryland, College Park, MD 20742, USA. [4]Department of Physics and Center for Theory of Quantum Matter, University of Colorado Boulder, Boulder, CO 80309, USA. [5]These authors contributed equally: Yixing Fu, Elio J. König, Justin H. Wilson. ✉email: jed.pixley@physics.rutgers.edu

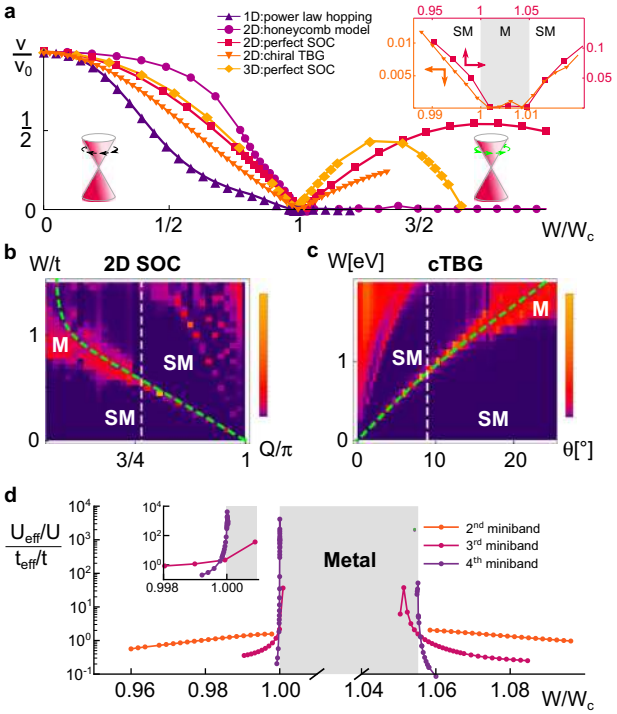

Fig. 1 Magic-angle transition. A quasiperiodic potential or tunneling generically drives an eigenstate quantum phase transition from a semimetal (SM) to metal (M). **a** For many models, the velocity at the Dirac node v decreases with the strength of the potential W until it reaches $v = 0$ at the transition, W_c; this is an indication of the flattening of the bands. In some cases an intermediate metallic phase (see inset) separates a reentrant semimetal with a reversed helicity (depicted by the Dirac cones). **b**, **c** We construct a phase diagram in terms of potential strength W (interlayer tunneling for cTBG) and quasiperiodic modulation Q (twist angle θ for cTBG) by computing the density of states at zero energy $\rho(0)$; analytical perturbative results (see Eq. (4), Supplementary Notes 3 and refs. [17,30]) are represented by the green dashed lines. Cuts along the dashed white lines are presented in Fig. 2c, d. Color bars represent $\rho(0)$ and with widths **b** 5, and **c** 1.25 and dark purple represents the value 0 on both. **d** An infinite number of semimetal minibands form as the transition is approached; each has higher effective interaction than the last as we approach the transition. For 2D SOC, we construct exponentially localized Wannier states on the first four minibands (see Fig. 4) leading to a model with an effective, strongly renormalized Hubbard interaction $U_{\rm eff}/t_{\rm eff}$ in terms of the bare interaction U/t.

Generalizing the physics of the first magic angle of TBG to magic-angle semimetals results in the phenomena summarized by Fig. 1. First, increasing W quenches the kinetic energy, reducing the Dirac velocity v until it ultimately reaches zero at the single-particle quantum critical point (where the DOS becomes nonanalytic). The velocity vanishes in a universal manner characterized by critical exponents that are distinct in each dimension. Second, the DOS and wave functions display a transition from a ballistic semimetal to a metallic phase; this is a so-called "unfreezing" transition in momentum space, which represents a non-standard form of delocalization[33]. For a subset of magic-angle semimetals (including Eqs. (2) and (3)), the semimetal reenters at a second transition W_c' with a reversed sign of the helicity at each Dirac node[34]; for general Q (or θ), multiple semimetal-metal-semimetal transitions can appear as W is tuned, see Fig. 1b, c. Third, the quenched kinetic energy implies a divergence of the dimensionless interaction coupling constant, Fig. 1d, leading to exotic many-body states. Importantly, these effects occur generically under the necessary condition that the quasiperiodic modulation respects the symmetries which protect the semimetallic touching points (see Supplementary Note 3).

Effective models

A variety of effective models (defined in Supplementary Note 1) illustrate our proposal. Here, we focus on two models: a 2D tight-binding Hamiltonian of "perfect" spin-orbit coupling (SOC) on a square lattice and a lattice model of TBG at moderate twist angles ($\theta \approx 9^\circ$) in the chiral limit (cTBG) that disallows interlayer tunneling between equivalent sub-lattices[30] (we fix the bare lattice spacing to unity and $\hbar = 1$). Nonetheless, our main conclusions also apply to TBG beyond the chiral limit for similar twist angles. (Here, we consider the chiral limit of TBG as it provides the clearest presentation of magic-angle criticality but such a transition can also be shown to persist in the full TBG model. This study will appear elsewhere). The SOC model is given by a hopping $\hat{T}_{\rm SOC} = t/2\sum_{\mathbf{r},\mu}(ic_{\mathbf{r}}^\dagger \sigma_\mu c_{\mathbf{r}+\hat{\mu}} + \text{h.c.})$ and a quasiperiodic potential

$$\hat{V}_{\rm SOC} = W \sum_{\mathbf{r},\mu=\mathbf{x},\mathbf{y}} \cos(Qr_\mu + \phi_\mu) c_{\mathbf{r}}^\dagger c_{\mathbf{r}}, \tag{2}$$

where the σ_μ are Pauli matrices, $c_{\mathbf{r}}$ are two-component annihilation operators, t is the hopping strength, and ϕ_μ is the offset of the origin. The lattice model that captures the low-energy theory of cTBG at incommensurate twist angles contains $\hat{T}_{\rm cTBG}$ that describes nearest neighbor hopping (amplitude $t = 2.8$ eV) on the honeycomb lattice. The interlayer tunneling in the chiral limit is given by:

$$\hat{V}_{\rm cTBG} = W\sum_{\mathbf{r},\mu}\Big[\cos(\mathbf{q}_\mu \cdot \tfrac{\mathbf{r}+\mathbf{r}_\mu}{2} + \phi_\mu) c_{1A\mathbf{r}_\mu}^\dagger c_{2B\mathbf{r}} - \sum_{n=1}^{6} \tfrac{(-1)^n}{3\sqrt{3}} \sin(\mathbf{q}_\mu \cdot \tfrac{\mathbf{r}+\mathbf{r}_{\mu n}}{2} + \phi_\mu) c_{1A\mathbf{r}_{\mu n}}^\dagger c_{2B\mathbf{r}} + (A \leftrightarrow B)\Big] + \text{h.c.}, \tag{3}$$

where $c_{lA/B\mathbf{r}}$ annihilates an electron on layer l, sublattice A/B, and position $\mathbf{r}$. The index $\mu = 1, 2, 3$ labels nearest neighbors such that $\mathbf{r}_1 - \mathbf{r} = (0, 1)$ [$\mathbf{q}_1 = k_\theta(0, -1)$] with $\mathbf{r}_\mu - \mathbf{r}$ [$\mathbf{q}_\mu$] being 120° rotations of the previous vector. The positions $\mathbf{r}_{\mu n} = \mathbf{r}_\mu + \mathbf{a}_n$ where $\mathbf{a}_1 = (\sqrt{3}/2, 3/2)$ and each subsequent $\mathbf{a}_n$ is a 60° rotation of the last (i.e., labeling nearest neighbors on the triangular Bravais lattice). Last, $|\mathbf{q}_\mu| = k_\theta = \frac{8\pi}{3\sqrt{3}}\sin(\theta/2)$ encodes the twist angle, and $\sum_\mu \phi_\mu = 0$ to satisfy C_6 symmetry. Typically the offsets ϕ_μ in either model are averaged over. The kinetic part $\hat{T}_{\rm SOC}$ ($\hat{T}_{\rm cTBG}$) has a momentum space dispersion with four (two) Dirac nodes and a velocity $v_0 = t$ ($v_0 = 3t/2$), see Fig. 2a, b inset. Returning to Eq. (2), we see that Q replaces the role of the twist angle in Eq. (3); unless otherwise stated, we highlight incommensurate effects by taking $Q = 2\pi/\varphi^2$ ($\theta = 2\arcsin(\sqrt{3}/2\varphi^5) \approx 8.96^\circ$) where φ is the golden ratio, and in numerical simulations we employ rational approximants $Q_n \equiv 2\pi F_{n-2}/F_n$ (k_θ is approximated using continued fractions, see Supplementary Note 1 for details) where the system size $L = F_n$ is given by the nth Fibonacci number[34]. Other values, in particular smaller π—Q and θ, are discussed in the Supplementary Information and below. In the low-energy approximation this model is identical to the continuum model studied in ref. [30] where exact flat bands are uncovered and explained; this makes this model ideal to study incommensurate effects on the lattice.

In addition to Eqs. (2) and (3) we have studied a multitude of other d-dimensional models in an incommensurate potential: the π-flux model and the honeycomb model in 2D, a 3D variant of Eq. (2) (studied previously in ref. [34]), and a 1D long range hopping model with a power law dispersion $E = -t\ \text{sign}(\cos k)|\cos k|^\sigma$ with $\sigma < 1$[35]—in this 1D case, v is not a velocity (details on 1D case can be found in the last part of Supplementary Note 2). Each of these models generates flat bands and magic-angle physics similar to TBG. Importantly, these semimetallic 2D Dirac points have been realized in cold atomic setups using either a

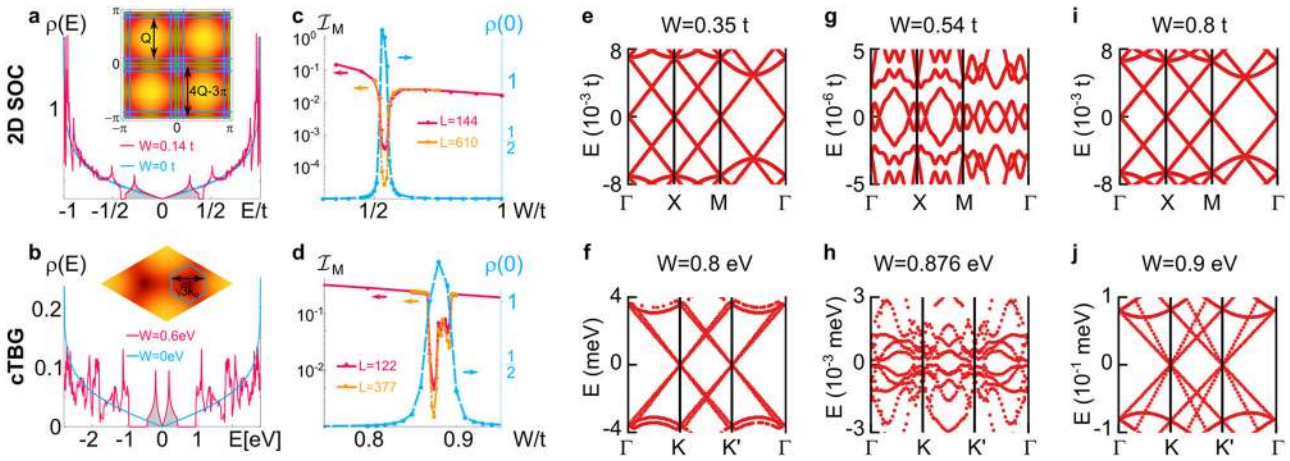

Fig. 2 Eigenstate transition as manifested in the single-particle spectrum. a, **b** DOS $\rho(E)$ in units of $(tL^2)^{-1}$ averaged over 300 realizations of phases ϕ_μ and random twisted boundary conditions (explained in more detail in Supplementary Note 2). The gray shading represents the number of states in the first miniband and matches the area of the mini-Brillouin zones around each Dirac point produced by the leading scattering vectors depicted in the inset of **a**, **b** (we chose a rhombic representation of the Brillouin zone of TBG such that $\mathbf{k} = k_1\mathbf{G}_1 + k_2\mathbf{G}_2$ for reciprocal lattice vectors $\mathbf{G}_{1,2}$ of graphene). **c**, **d** Cuts along the dashed white lines of the phase diagram in Fig. 1b, c, displaying $\rho(0)$ and $\mathcal{I}_M(q = 2, L)$ [Eq. (5)]. These illustrate sequences of semimetallic and metallic transitions concomitant with momentum space delocalization (see Fig. 3). The twist dispersions illustrate the difference between semimetallic phases (**e, i, f, j**) and the metallic phase (**g**, **h**) as well as the remarkably reduced bandwidths (note the reduced scale). The 2D SOC (cTBG) data were obtained for $Q = 2\pi F_{n-2}/F_n$ ($\theta = 2\arcsin(\sqrt{3}F_{n-5}/[2F_n])$) at $L = 144$ ($L = 377$) and KPM expansion order $N_C = 2^{12}$ ($N_C = 2^{13}$) in the calculation of the DOS while $L = 233$ in **e**–**j**.

honeycomb optical lattice[36,37] or artificial gauge fields[38–40], whereas the 1D model we consider can be realized using trapped ions[41]. The 3D variant of Eq. (2) is theoretically possible to implement[42–44], but has not been experimentally realized yet. In each of these experimental setups, quasiperiodic potentials can then be realized, e.g., by additional lasers[45], programmable potentials[46], or a digital mirror device[47]. Alternative emulators of Dirac semimetals can also be realized in metamaterials, e.g., in topolectrical circuits[7] or in arrays of electromagnetic microwave resonators[48]. Quasiperiodicity can then be encoded through the spatial modulation of the electrical circuit elements.

Single-particle spectrum and velocity renormalization

We first discuss the spectral characteristics of magic-angle semimetals probed through the DOS, defined as $\rho(E) = 1/N_H\sum_i\delta(E - E_i)$ where E_i is the ith eigenenergy and N_H is the size of the single-particle Hilbert space. At weak quasiperiodic modulation, the semimetal is stable, i.e., $\rho(E)$ vanishes at zero energy with the same power law as in the limit of $W = 0$, while hard spectral gaps and Van Hove singularities develop at finite energy. For Weyl and Dirac Hamiltonians the low-$|E|$ DOS obeys $\rho(E) \sim v^{-d}|E|^{d-1}$, and as W increases, the $(d-1)$st derivative of the DOS $[\rho^{(d-1)}(0) \propto 1/v^d]$ increases, see Fig. 2a, b for the model in Eqs. (2) and (3), respectively. These weak coupling features may be understood at the level of perturbation theory.

We find that gaps appear at finite energy due to the hybridization around Dirac nodes a distance Q (or $\sqrt{3}k_\theta$) away in momentum space, see the insets in Fig. 2a, b, inset. For the SOC (cTBG) model, this process "carves out" a square (hexagon) around each Dirac cone which contains $2[(\pi - Q)L/2\pi]^2$ ($4[3\sqrt{3}k_\theta L/4\pi]^2$) states. For a given incommensurate Q or θ, there is an infinite sequence of relevant orders in perturbation theory that produce quasi-resonances and open up gaps near zero energy, forming minibands; this is in contrast to the commensurate case when this sequence is finite. For example, for 2D SOC and $Q = 2\pi/\varphi^2$, the infinite sequence is given by half the even Fibonacci numbers $F_{3n}/2$, which is the sequence 1, 4, 7, 72, 305, … (see Supplementary Note 3). In the incommensurate limit, near the magic-angle transition this sequence of gaps produces a corresponding sequence of minibands, shown in Fig. 1d for the second, third, and fourth. We explore the effect of this sequence of minibands using superlattices in "Commensurate superlattices and Hubbard models".

Similar to TBG, the renormalization of the velocity in the 2D SOC model can be analytically determined using fourth-order perturbation theory (details in Supplementary Note 3)[17]. In terms of the dimensionless coupling constant $\alpha = W/[2t\sin(Q)]$ for Eq. (2) this yields:

$$\frac{v(W)}{v(0)} = \frac{1 - 2\alpha^2[1 - \cos(Q)] + \alpha^4\frac{4 - 5\cos(Q) + 6\cos(2Q)}{\cos(Q)}}{1 + 4\alpha^2 + \alpha^4\{16 + [2 + 1/\cos(Q)]^2\}}. \quad (4)$$

The root of the numerator captures the first magic-angle transition line well when $Q > \pi/2$, see Fig. 1b, independently of whether Q is commensurate or incommensurate. To describe additional magic-angles, as observed in our numerical data in Fig. 1b, c, higher order perturbation theory is required. For reentrant semimetallic phases, Eq. (4) indicates the reversal of the Berry phase, consistent with the inversion of miniband states in 3D[34]. In each model we have considered for $d > 1$, we have found that the perturbative expression for the velocity (summarized in Supplementary Table 1) has a magic-angle condition where the velocity vanishes.

As the magic-angle is approached, higher perturbative corrections become relevant. To go beyond perturbation theory, we compute the DOS using the numerically exact kernel polynomial method (KPM), on sufficiently large system sizes across a range of models of various dimensions. At a critical $\alpha = \alpha_c \sim 1$ the DOS becomes nonanalytic and a metallic spectrum with finite $\rho(0)$ develops for $\alpha > \alpha_c$, see Fig. 2c, d (for cTBG $\alpha = \frac{W}{2t\sin(3k_\theta/4)}$). In particular, for $d > 1$ and fixed Q or θ, $\rho(E) \sim |W - W_c|^{-\beta}|E|^{d-1}$ implying the velocity $v(W) \sim |W - W_c|^{\beta/d}$. Surprisingly, we find $\beta \approx 2$ in each model investigated above 1D (see Supplementary Note 2)[34], indicating that this exponent is universal. In 1D, this magic-angle effect also exists but is modified by the form of the dispersion such that $\rho(E) \sim |W - W_c|^{-\beta}|E|^{1/\sigma - 1}$, and for the case $\sigma = 1/3$ we find $\beta = 4.0 \pm 0.8$.

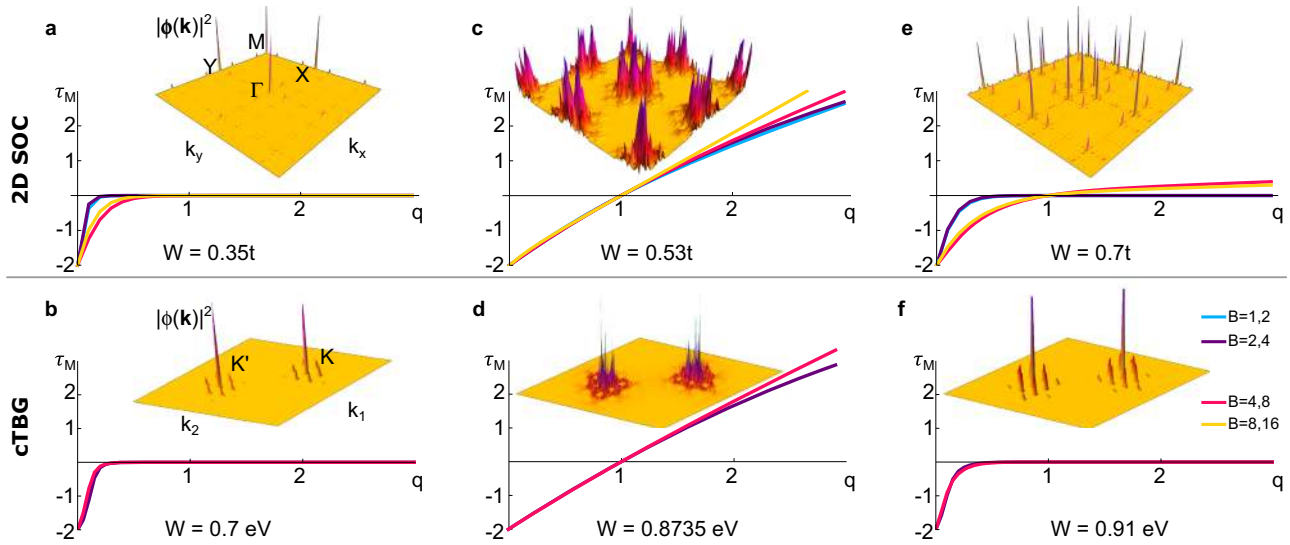

Fig. 3 Eigenstate transition as manifested in momentum space wave functions at the Dirac node energy $E = 0$. a–f Wave function characteristics as described by the scaling exponent $\tau_M(q)$ averaged over 100 random phases and twisted boundary conditions. For $W < W_c$ and $W > W_c'$ the wave functions are ballistic [with a frozen $\tau_M(q)$] while for $W_c < W < W_c'$ they are critical in momentum space [$\tau_M(q)$ is weakly non-linear in q]. Inset of **a**–**f** corresponding momentum space wave functions. The 2D SOC (cTBG) data were obtained for $Q = 2\pi F_{n-2}/F_n$ ($\theta = 2\arcsin(\sqrt{3}F_{n-5}/[2F_n])$) at $L = 144$ ($L = 377$).

This velocity renormalization is the manifestation of the aforementioned reconfiguration of the band structure and the appearance of a sequence of minibands. Of course, broken translational symmetry precludes a standard band structure of dispersive Bloch waves. In Fig. 2e–j, we therefore illustrate this reconfigured band structure, at a fixed rational approximant, in the form of the twist dispersion (obtained by exact diagonalization in the presence of twisted boundary conditions) along high symmetry lines for the models defined in Eqs. (2), (3). We performed the analogous analysis for a multitude of models and plotted the velocity $v(W)$ near the semimetallic touching points in Fig. 1a. The velocity $v(W)$ as determined by computing the twist dispersion agrees with the calculation of $\rho^{(d-1)}(0)$, see Supplementary Note 2.

Critical single-particle wave functions

Magic-angle semimetals are intimately linked to the physics of Anderson transitions in momentum space; this is captured by the eigenfunctions near the Dirac node energy, $E = 0$[34].

We compute the low-energy wave functions using Lanczos for large L reaching up to $L = 377$ and 610 in the cTBG and SOC models, respectively. Qualitatively, we find that the structure of the wave functions in the semimetallic phase is stable and adiabatically connected to the ballistic $W = 0$ limit, with isolated ballistic spikes in momentum space, see Fig. 3a, b. In contrast, the form of the wave functions is completely different in the metallic state, see Fig. 3c, d, as it appears delocalized both in momentum and real space with non-trivial structure (see details in Supplementary Note 5). Finally, in the reentrant semimetal, the wave functions are again ballistic, see Fig. 3e, f. Crucially, in all models that we studied, the positions of the transitions in the spectral properties of the DOS coincide with the transitions of the wave functions characteristics within numerical resolution, see Fig. 2c, d.

In order to quantify the eigenstate QPTs of the wave functions, we generalize the multifractal wave function analysis[33] to momentum space. We define the inverse participation ratio of the energy eigenstates in momentum space[34] $\psi_E(\mathbf{k})$ at a given energy E:

$$\mathcal{I}_M(q,L) = \sum_{\mathbf{k}} |\psi_E(\mathbf{k})|^{2q} \sim L^{-\tau_M(q)}. \tag{5}$$

We can now apply properties of the scaling exponent $\tau_M(q)$, typically used to analyze real space localization, to momentum space. It monotonically increases [obeying $\tau_M(0) = -d$ and $\tau_M(1) = 0$] and distinguishes delocalized wave functions [$\tau_M(q) = d(q-1)$] from exponentially localized peaks [$\tau_M(q>0) = 0$] and critical states with non-linear "multifractal" $\tau_M(q)$. A variant of multifractal states, which are called "frozen," display $\tau_M(q > q_c) = 0$ for a given $q_c \in (0, 1]$; their peak height is system size independent, as in standard localized states, but show multifractal correlations in their tails[33]. We employ the standard binning technique (varying the binning size B) to numerically extract the scaling exponents $\tau_M(q)$ in systems of a given finite size, see Supplementary Note 5 for details.

Focusing on $q = 2$, as shown in Fig. 2c, d for the SOC and cTBG models, respectively, the momentum space wave function at the Dirac node energy delocalizes upon crossing the magic-angle in the incommensurate limit. The momentum space delocalization can not occur in the commensurate case; Bloch's theorem ensures the existence of states with well defined (i.e., well localized) crystalline momenta. For example, consider Eq. (2) in the commensurate limit where $Q/2\pi = a/b$ (a and b are coprime integers). In this case, $\mathcal{I}_M(q,L)$ is bounded from below by $1/b^{d(q-1)}$ and hence $\tau_M(q) = 0$ in the thermodynamic limit $L/b \to \infty$ preventing momentum space delocalization (see Supplementary Note 5). In contrast, we here numerically access the incommensurate limit using finite size scaling of rational approximants corresponding to $L = b \to \infty$.

The scaling analysis of $\mathcal{I}_M(q,L)$ at the energy of the Dirac node $E = 0$, presented in Fig. 3a–f for Eqs. (2) and (3), demonstrates three phases of distinct wave function structures in momentum space. A frozen spectrum $\tau_M(q)$ occurs in the two semimetal regimes. In sharp contrast, the function $\tau_M(q)$ unfreezes in the metallic phase with finite $\rho(0)$. Surprisingly, throughout the metallic phase the spectra appear to be weakly multifractal in both momentum and real space (Supplementary Note 5), we find for the SOC model that $\tau_M(q) \approx 2(q-1) - 0.25q(q-1)$ and for the cTBG model we obtain $\tau_M(q) \approx 2(q-1) - 0.15q(q-1)$ (in the

region $|q| < 1$ and within the limits of our numerical precision) in Fig. 3c, d, which are both non-linear in q. The observation of similar behavior in all models that we investigated (as listed in Supplementary Note 1) corroborates the interpretation of the magic-angle phenomenon in the incommensurate limit as one of eigenstate quantum criticality and generalizes the quasiperiodic 3D Weyl semimetal-to-diffusive metal QPT[34] to arbitrary dimensions. In two dimensions, we do not find any signatures of diffusion (consistent with the marginality of two dimensions[49,50]) and in one dimension the semimetal transitions directly to an Anderson insulator (shown in Supplementary Note 2). Lastly, when $d > 1$ and W is substantially larger than the magic-angle transition, all investigated models undergo Anderson localization in real space (e.g., at $W > 1.75t$ in the case of the 2D SOC model at $Q = 2\pi/\varphi^2$).

Commensurate superlattices and Hubbard models

So far, our analysis regarded non-interacting magic-angle semimetals in the strict incommensurate limit. We now turn to the interparticle interaction term $\hat{U}$ in the Hamiltonian in Eq. (1) in commensurate superlattices. In order to illustrate how the appearance of flat bands enhances correlations, we construct a series of emergent Hubbard models near the magic-angle transition for Eq. (2) at $\phi_\mu = \pi/2$ supplemented by:

$$\hat{U}_{SOC} = U\sum_{\mathbf{r}} n_{\mathbf{r},\uparrow} n_{\mathbf{r},\downarrow}, \tag{6}$$

with $n_{\mathbf{r}\sigma} = c^\dagger_{\mathbf{r}\sigma} c_{\mathbf{r}\sigma}$. In contrast to the previous discussion, we take commensurate approximations in order to build translationally invariant Hubbard models. In particular, we still use the rational approximants $Q_n = 2\pi F_{n-2}/F_n$, only now we take the size of the system $L = mF_n$ for some integer m, effectively taking the thermodynamic limit in L before the limit of quasiperiodicity $Q_n \to Q$. This is reminiscent of moiré lattices used to model TBG, and similarly, we can unambiguously define a supercell of size $\ell = F_n$ and isolate bands in k-space.

In particular, these bands are intimately related to the hierarchy of minibands derived with perturbation theory: when $\ell = F_{3a+b}$ for integers a and $b = 1, 2$, the gap for the central band opens at order $F_{3a}/2$ in perturbation theory (for $\ell = F_{3a}$, the Dirac nodes gap at order $F_{3a}/2$. See Supplementary Note 3 for details). The series of superlattices indicated by ℓ correspond to the sequence of gap openings in "Single-particle spectrum and velocity renormalization"—making the notion precise—with (downfolded) Brillioun zones depicted in Fig. 4b. Near W_c, hard gaps open and the minibands form as illustrated in Fig. 4a for $\ell = 13$, 55, 233 (respectively, the 2nd, 3rd, and 4th minibands). We conjecture that all of these minibands (as $\ell \to \infty$) achieve gaps near W_c as evidenced by Fig. 4a, c in the incommensurate limit, indicating something akin to the singular continuous spectrum of the Aubry–André model at criticality[51]. Furthermore, the central band becomes flatter, as indicated by the reduction in bandwidth seen in Fig. 4c which we track until the dispersion loses its semimetallic character.

We exploit this miniband formation and the existence of hard gaps to build symmetric Wannier functions in the semimetallic regime, see Fig. 4d. To build the Hubbard models, we perform approximate joint diagonalization on the position operators $(\hat{x}_\mu)$ projected (with projection operator P) onto a given band $\hat{X}^{\mathrm{MB}}_\mu \equiv P\hat{x}_\mu P$ in order to determine the Wannier states[52] (for details and code, see Supplementary Note 6). We have checked that not only are the computed Wannier states exponentially localized to numerical precision (Fig. 4d, inset), but that they are also symmetric. Therefore, the minibands formed from the SOC model and pictured in Fig. 4 are not topological[53], fragile[54,55] or otherwise.

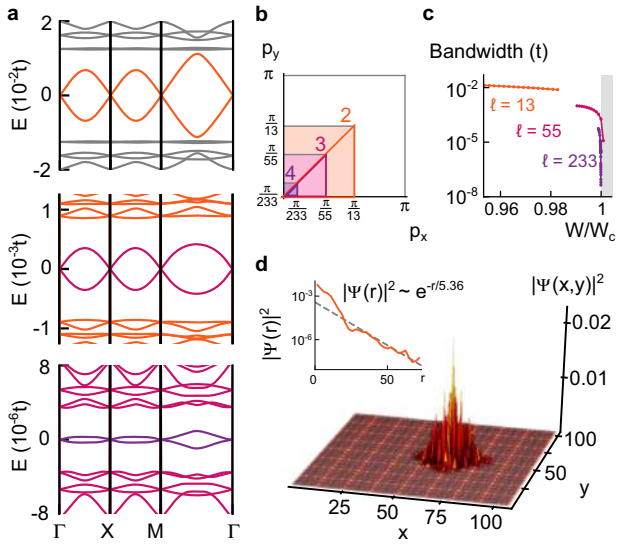

Fig. 4 Supercell analysis and Wannier functions. The color coding matched across **a**–**c** (and Fig. 1d) indicates the second (orange), third (maroon), and fourth (purple) minibands. **a** The dispersion of Eq. (2) in the mini-Brillouin zone for superlattices $(\ell, W) = (13, 0.5)$, $(\ell, W) = (55, 0.5244)$, $(\ell, W) = (233, 0.5244)$ (from top to bottom); this illustrates successive emergence of minibands (from top-to-bottom) as a consequence of consecutive downfoldings of the Brillouin zone. **b** The corresponding mini-Brillouin zones (logarithmic scale). **c** The dramatic reduction in bandwidth near the critical point for each miniband. **d** For $(\ell, W) = (13, 0.5)$ and $L = 104$, computed Wannier function $\psi(x, y)$ that is sitting upon the local density of states $\rho_{\mathrm{band}}(\mathbf{r}) = \sum_n |\langle \mathbf{r}|\mathbf{E_n}\rangle|^2$ (shown as a density plot) for eigenstates of the (orange) band $|E_n\rangle$, on a 104×104 lattice. (Inset). The exponential localization of the Wannier state.

As a clear example, when $W = 0.5t$ and $(\ell, m) = (13, 8)$, we see a clear band around $E = 0$ in Fig. 4a, and we find Wannier centers in a well-defined grid (Fig. 4d, main panel) corresponding to exponentially localized Wannier states (Fig. 4d, inset). The projected Hamiltonian has the approximate form of Eqs. (2) and (6) with a renormalized U_{eff}, t_{eff} and $W_{\mathrm{eff}} = 0$. With this approach, we can identify successive gaps leading up to the metallic transition from either side along with dramatic enhancements of interactions, which reach up to a massive $U_{\mathrm{eff}}/t_{\mathrm{eff}} \sim 4100U/t$ for the fourth miniband with supercell $\ell = 377$, as shown in Fig. 1d. This can also been shown analytically using a one-step renormalization group calculation, which yields the divergence $U_{\mathrm{eff}}/t_{\mathrm{eff}} \sim U(1/\ell)^{d-1} Z^2/v \sim 1/|W - W_c|$, ($\sqrt{Z}$ is the wave function renormalization), as shown in detail in Supplementary Note 3. Due to finite size, the apparent location of W_c can artificially shift, therefore in Fig. 1d we use $W_c = \tilde{W}_c \frac{\sin Q}{\sin Q_n}$ where $\tilde{W}_c$ is the transition point when $n \to \infty$. In Supplementary Fig. 16, we present the data for a large set of (ℓ, m) corroborating our findings.

Away from $E = 0$, nearly flat (semimetallic) bands can form well before the magic-angle transition with similarly large $U_{\mathrm{eff}}/t_{\mathrm{eff}}$, see Fig. 4a. In very close proximity to the transition, multi-orbital Hubbard models appear (see Supplementary Note 6).

Experimental cold atomic realization

All sufficient ingredients for emulating magic-angle phenomenon are available in ultracold atomic gas and metamaterial[48,56] experiments. In particular for ultracold atomic gases, to probe fermionic strong correlations, the atomic species ^{40}K and ^{6}Li are prime candidates; we estimate that the underlying lattice can be relatively shallow (around eight lattice recoil energies), and need temperatures relative to the Fermi temperature (of the entire gas) $T/T_F \approx 0.25$ to ensure fermion population fills but does not exceed

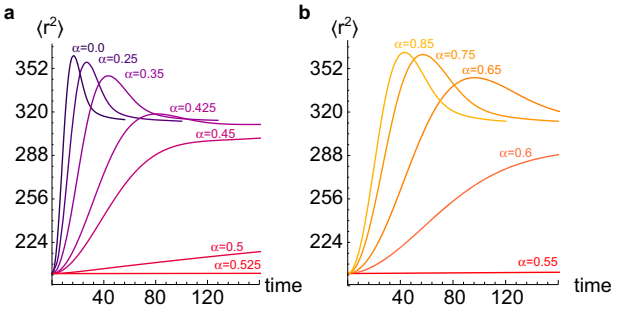

Fig. 5 Boltzmann wave packet spreading. Spreading of the mean square radius $\langle r^2\rangle = \Sigma_{\mathbf{r}} \mathbf{r}^2 \rho(\mathbf{r})$ of the particle density $\rho(\mathbf{r})$ as a function of time in units of the inverse hopping rate $1/t$ (**a** $\alpha < \alpha_c$, **b** $\alpha > \alpha_c$). Here, we consider the interacting 2D SOC model, Eqs. (2) and (6), and we employ Eq. (4) to incorporate the magic-angle effect (occurring at $\alpha_c \approx 0.53$ in this approximation) into a semianalytical hydrodynamic treatment. The initial steady state at finite temperature is defined by a particle [energy] density $\rho(\mathbf{r}) = e^{-\mathbf{r}^2/[2\xi^2]}/\xi^2$ $[\rho_E(\mathbf{r}) = v_0\left(1 + 3e^{-\mathbf{r}^2/\xi^2}\right)/\xi^3]$, with $v_0 \equiv v(\alpha = 0)$ is the bare velocity and we chose $\xi = 4$ for the initial spread of the density profile. The hydrodynamic equations were numerically solved in the presence of an onsite repulsion $U(\alpha = 0) = 0.025t$ and Umklapp scattering rate $1/\tau(\alpha = 0) = 0.0075t$ (see Supplementary Note 4).

the first miniband. To see large correlations, trap sizes should accommodate at least roughly 30×30 optical lattice sites. In addition to any spectroscopic measurements that probe the DOS (e.g., radiofrequency spectroscopy[57]), we propose and demonstrate (in more detail in Supplementary Note 4) that the analysis of wave packet dynamics is an indicator of magic-angle physics. In the absence of interactions, we numerically predict a non-monotonic spreading of the wave function for increasing W (see Supplementary Fig. 10) in the regime with multiple magic angles. We have also studied the interacting model in the hydrodynamic regime by using a generalization of the Boltzmann kinetic equation[58] (see details in Supplementary Note 4). Its solution confirms the drastic decrease of the expansion velocity and a substantial enhancement of diffusive dynamics near the magic angle, see Fig. 5. The observation of these effects is possible within experimentally realistic observation time of $50t^{-1}$ (~10–100 ms). Moreover, our work demonstrates an experimental protocol for realizing strong correlations by first cooling the gas to quantum degeneracy and then applying a quasiperiodic potential to create flat bands without the need to cool the system in a Mott insulator phase or load the atoms into a flat band.

DISCUSSION

In summary, we introduced a class of magic-angle semimetals and demonstrated the general appearance of a single-particle QPT in the incommensurate limit at which, simultaneously, (1) the kinetic energy vanishes universally, (2) a non-zero DOS appears at zero energy, and (3) the wave functions display delocalization and multifractality in momentum space. In the presence of interactions we demonstrated that this eigenstate criticality leads to a strongly correlated Hubbard model by computing Wannier states on a superlattice. Lastly, we presented a detailed discussion of an experimental realization in cold atomic quantum emulators.

Regarding experimentally realized twisted graphene heterostructures at much smaller twist angles than we have considered here ($\theta \approx 1.1°$), it has not been obvious whether incommensuration is an important ingredient[59]. Quasiperiodic effects rely upon weakly detuned processes at which the total transferred momentum wraps the Brillouin zone. In contrast, the momentum transfer induced by scattering off a small angle superstructure is minute. Therefore—it is often concluded—both effects of incommensurability and intervalley scattering are negligible as processes in higher order perturbation theory. As our numerics demonstrate, this results in the suppression of the width of the metallic sliver in Fig. 1b, c that scales like $W_c' - W_c \sim \theta^3$, making observing such a metallic phase exceedingly difficult at small twist angles. Nonetheless, we expect Anderson delocalization in momentum space even at small twist angles. This is because this physics is dominated by rare resonances (as manifested in the locator expansion[60]) and controlled by α, while perturbative processes are parameterized by W/t and are therefore small. Furthermore, the contiguous phase boundary in Fig. 1b, c may imply that the physics of small angles directly connects to large, incommensurate twists[61–63]. However, within present day numerics, we cannot exclude that this boundary of eigenstate phase transitions terminates at a finite, small angle, which would imply the existence of a critical Anderson delocalization end point in Fig. 1b, c. The coexistence of finite DOS with other features of this phase at larger angles suggests that the phase extends to $\theta \to 0$ ($Q \to \pi$), but an end point is appealing as it would establish a theoretical paradigm of quasiperiodic Anderson tricriticality. Any rational approximant or commensurate angle truncates the infinite sequence of resonances and minibands which leads to a rounding of the QPT (akin to finite size effects in usual transitions) and the absence of momentum space delocalization. The amplified interactions due to flat bands and an enhanced DOS occur for both incommensurate and commensurate cases as Fig. 1d demonstrates. This enhancement coupled with eigenstate quantum criticality in the incommensurate limit characterizes magic-angle semimetals, including TBG at moderate twist angles.

Note Added: While this manuscript was under consideration following its announcement in arXiv:1809.04604, independent proposals to simulate twistronics in cold atoms appeared and were published in refs. [64,65].

METHODS

Numerical methods

The numerical methods used are the KPM[66] for the DOS, exact diagonalization and Lanczos for eigenstates, approximate joint diagonalization for Wannier functions[67], and numerical partial differential equation solvers for the Boltzmann kinetics. These methods are explained in context in the Results section with additional details in the Supplementary information, particularly Supplementary Notes 2, 4, 5, and 6.

DATA AVAILABILITY

The data sets generated during and/or analyzed during the current study are available from the corresponding author on reasonable request.

CODE AVAILABILITY

The numerical code used to generate these data are available upon request. For Wannier functions, the code used for the approximate joint diagonalization can be found here https://github.com/jhwilson/AJD.jl.

Received: 2 April 2020; Accepted: 9 September 2020;
Published online: 06 October 2020

REFERENCES

1. Xu, S.-Y. et al. Topological phase transition and texture inversion in a tunable topological insulator. *Science* **332**, 560–564 (2011).
2. Lindner, N. H., Refael, G. & Galitski, V. Floquet topological insulator in semiconductor quantum wells. *Nat. Phys.* **7**, 490–495 (2011).
3. Burkov, A. & Balents, L. Weyl semimetal in a topological insulator multilayer. *Phys. Rev. Lett.* **107**, 127205 (2011).
4. Belopolski, I. et al. A novel artificial condensed matter lattice and a new platform for one-dimensional topological phases. *Sci. Adv.* **3**, e1501692 (2017).

5. Dalibard, J., Gerbier, F., Juzeliūnas, G. & Öhberg, P. Colloquium: artificial gauge potentials for neutral atoms. *Rev. Mod. Phys.* **83**, 1523–1543 (2011).
6. Aidelsburger, M., Nascimbene, S. & Goldman, N. Artificial gauge fields in materials and engineered systems. *C. R. Phys.* **19**, 394–432 (2018).
7. Lee, C. H. et al. Topolectrical circuits. *Commun. Phys.* **1**, 39 (2018).
8. Ozawa, T. et al. Topological photonics. *Rev. Mod. Phys.* **91**, 015006 (2019).
9. Cao, Y. et al. Correlated insulator behaviour at half-filling in magic-angle graphene superlattices. *Nature* **556**, 80–84 (2018).
10. Chen, G. et al. Evidence of a gate-tunable Mott insulator in a trilayer graphene moiré superlattice. *Nat. Phys.* **15**, 237–241 (2019).
11. Cao, Y. et al. Unconventional superconductivity in magic-angle graphene superlattices. *Nature* **556**, 43–50 (2018).
12. Yankowitz, M. et al. Tuning superconductivity in twisted bilayer graphene. *Science* **363**, 1059–1064 (2019).
13. Song, J. C. W., Shytov, A. V. & Levitov, L. S. Electron interactions and gap opening in graphene superlattices. *Phys. Rev. Lett.* **111**, 266801 (2013).
14. Kim, K. et al. Tunable moiré bands and strong correlations in small-twist-angle bilayer graphene. *Proc. Natl Acad. Sci. USA* **114**, 3364–3369 (2017).
15. Wu, F., Lovorn, T., Tutuc, E. & MacDonald, A. H. Hubbard model physics in transition metal dichalcogenide moiré bands. *Phys. Rev. Lett.* **121**, 026402 (2018).
16. Trambly de Laissardiere, G., Mayou, D. & Magaud, L. Localization of Dirac electrons in rotated graphene bilayers. *Nano Lett.* **10**, 804–808 (2010).
17. Bistritzer, R. & MacDonald, A. H. Moiré bands in twisted double-layer graphene. *Proc. Natl Acad. Sci. USA* **108**, 12233–12237 (2011).
18. dos Santos, J. L., Peres, N. & Neto, A. C. Continuum model of the twisted graphene bilayer. *Phys. Rev. B* **86**, 155449 (2012).
19. San-Jose, P., González, J. & Guinea, F. Non-abelian gauge potentials in graphene bilayers. *Phys. Rev. Lett.* **108**, 216802 (2012).
20. Li, G. et al. Observation of Van Hove singularities in twisted graphene layers. *Nat. Phys.* **6**, 109–113 (2010).
21. Brihuega, I. et al. Unraveling the intrinsic and robust nature of van Hove singularities in twisted bilayer graphene by scanning tunneling microscopy and theoretical analysis. *Phys. Rev. Lett.* **109**, 196802 (2012).
22. Kim, Y. et al. Charge inversion and topological phase transition at a twist angle induced van Hove singularity of bilayer graphene. *Nano Lett.* **16**, 5053–5059 (2016).
23. Padhi, B., Setty, C. & Phillips, P. W. Doped twisted bilayer graphene near magic angles: proximity to Wigner crystallization, not Mott insulation. *Nano Lett.* **18**, 6175–6180 (2018).
24. Po, H. C., Zou, L., Vishwanath, A. & Senthil, T. Origin of Mott insulating behavior and superconductivity in twisted bilayer graphene. *Phys. Rev. X* **8**, 031089 (2018).
25. Yuan, N. F. Q. & Fu, L. Model for the metal-insulator transition in graphene superlattices and beyond. *Phys. Rev. B* **98**, 045103 (2018).
26. Kang, J. & Vafek, O. Symmetry, maximally localized Wannier states, and a low-energy model for twisted bilayer graphene narrow bands. *Phys. Rev. X* **8**, 031088 (2018).
27. Xu, C. & Balents, L. Topological superconductivity in twisted multilayer graphene. *Phys. Rev. Lett.* **121**, 087001 (2018).
28. Lian, B., Wang, Z. & Bernevig, B. A. Twisted bilayer graphene: a phonon-driven superconductor. *Phys. Rev. Lett.* **122**, 257002 (2019).
29. Dodaro, J. F., Kivelson, S. A., Schattner, Y., Sun, X. Q. & Wang, C. Phases of a phenomenological model of twisted bilayer graphene. *Phys. Rev. B* **98**, 075154 (2018).
30. Tarnopolsky, G., Kruchkov, A. J. & Vishwanath, A. Origin of magic angles in twisted bilayer graphene. *Phys. Rev. Lett.* **122**, 106405 (2019).
31. Wolf, T. M. R., Zilberberg, O., Levkivskyi, I. & Blatter, G. Substrate-induced topological minibands in graphene. *Phys. Rev. B* **98**, 125408 (2018).
32. Janot, C. *Quasicrystals: A Primer*. *Monographs on the Physics and Chemistry of Materials* (OUP Oxford, 2012).
33. Evers, F. & Mirlin, A. D. Anderson transitions. *Rev. Mod. Phys.* **80**, 1355–1417 (2008).
34. Pixley, J. H., Wilson, J. H., Huse, D. A. & Gopalakrishnan, S. Weyl semimetal to metal phase transitions driven by quasiperiodic potentials. *Phys. Rev. Lett.* **120**, 207604 (2018).
35. Gärttner, M., Syzranov, S., Rey, A., Gurarie, V. & Radzihovsky, L. Disorder-driven transition in a chain with power-law hopping. *Phys. Rev. B* **92**, 041406 (2015).
36. Tarruell, L., Greif, D., Uehlinger, T., Jotzu, G. & Esslinger, T. Creating, moving and merging Dirac points with a Fermi gas in a tunable honeycomb lattice. *Nature* **483**, 302–305 (2012).
37. Jotzu, G. et al. Experimental realization of the topological Haldane model with ultracold fermions. *Nature* **515**, 237–240 (2014).
38. Aidelsburger, M. et al. Measuring the Chern number of Hofstadter bands with ultracold bosonic atoms. *Nat. Phys.* **11**, 162–166 (2015).
39. Huang, L. et al. Experimental realization of two-dimensional synthetic spin–orbit coupling in ultracold Fermi gases. *Nat. Phys.* **12**, 540–544 (2016).
40. Wu, Z. et al. Realization of two-dimensional spin-orbit coupling for bose-einstein condensates. *Science* **354**, 83–88 (2016).
41. Richerme, P. et al. Non-local propagation of correlations in quantum systems with long-range interactions. *Nature* **511**, 198 (2014).
42. Sun, K., Liu, W. V., Hemmerich, A. & Das Sarma, S. Topological semimetal in a fermionic optical lattice. *Nat. Phys.* **8**, 67–70 (2012).
43. Jiang, J.-H. Tunable topological Weyl semimetal from simple-cubic lattices with staggered fluxes. *Phys. Rev. A* **85**, 033640 (2012).
44. Dubček, T. et al. Weyl points in three-dimensional optical lattices: synthetic magnetic monopoles in momentum space. *Phys. Rev. Lett.* **114**, 225301 (2015).
45. Schreiber, M. et al. Observation of many-body localization of interacting fermions in a quasirandom optical lattice. *Science* **349**, 842–845 (2015).
46. Smith, J. et al. Many-body localization in a quantum simulator with programmable random disorder. *Nat. Phys.* **12**, 907–911 (2016).
47. Weitenberg, C. et al. Single-spin addressing in an atomic Mott insulator. *Nature* **471**, 319–324 (2011).
48. Peterson, C. W., Benalcazar, W. A., Hughes, T. L. & Bahl, G. A quantized microwave quadrupole insulator with topologically protected corner states. *Nature* **555**, 346–350 (2018).
49. Abrahams, E., Anderson, P., Licciardello, D. & Ramakrishnan, T. Scaling theory of localization: absence of quantum diffusion in two dimensions. *Phys. Rev. Lett.* **42**, 673–676 (1979).
50. Devakul, T. & Huse, D. A. Anderson localization transitions with and without random potentials. *Phys. Rev. B* **96**, 214201 (2017).
51. Hiramoto, H. & Kohmoto, M. Electronic spectral and wavefunction properties of one-dimensional quasiperiodic systems: a scaling approach. *Int. J. Mod. Phys. B* **6**, 281–320 (1992).
52. Marzari, N., Mostofi, A. A., Yates, J. R., Souza, I. & Vanderbilt, D. Maximally localized wannier functions: theory and applications. *Rev. Mod. Phys.* **84**, 1419–1475 (2012).
53. Brouder, C., Panati, G., Calandra, M., Mourougane, C. & Marzari, N. Exponential localization of Wannier functions in insulators. *Phys. Rev. Lett.* **98**, 046402 (2007).
54. Cano, J. et al. Topology of disconnected elementary band representations. *Phys. Rev. Lett.* **120**, 266401 (2018).
55. Po, H. C., Watanabe, H. & Vishwanath, A. Fragile topology and wannier obstructions. *Phys. Rev. Lett.* **121**, 126402 (2018).
56. Rechtsman, M. C., Jeong, H.-C., Chaikin, P. M., Torquato, S. & Steinhardt, P. J. Optimized structures for photonic quasicrystals. *Phys. Rev. Lett.* **101**, 073902 (2008).
57. Gaebler, J. et al. Observation of pseudogap behaviour in a strongly interacting Fermi gas. *Nat. Phys.* **6**, 569–573 (2010).
58. Schneider, U. et al. Fermionic transport and out-of-equilibrium dynamics in a homogeneous Hubbard model with ultracold atoms. *Nat. Phys.* **8**, 213–218 (2012).
59. Mele, E. J. Commensuration and interlayer coherence in twisted bilayer graphene. *Phys. Rev. B* **81**, 161405 (2010).
60. Scardicchio, A. & Thiery, T. Perturbation theory approaches to Anderson and many-body localization: some lecture notes. Preprint at https://arxiv.org/abs/1710.01234 (2017).
61. Pal, H. K., Spitz, S. & Kindermann, M. Emergent geometric frustration and flat band in moiré bilayer graphene. *Phys. Rev. Lett.* **123**, 186402 (2019).
62. Yao, W. et al. Quasicrystalline 30° twisted bilayer graphene as an incommensurate superlattice with strong interlayer coupling. *Proc. Natl Acad. Sci. USA* **115**, 6928–6933 (2018).
63. Ahn, S. J. et al. Dirac electrons in a dodecagonal graphene quasicrystal. *Science* **361**, 782–786 (2018).
64. Salamon, T, et al. Simulating Twistronics without a Twist. *Phys. Rev. Lett.* **125**, 030504 (2020).
65. González-Tudela, A. & Cirac, J. I. Cold atoms in twisted-bilayer optical potentials. *Phys. Rev. A.* **100**, 053604 (2019).
66. Weiße, A., Wellein, G., Alvermann, A. & Fehske, H. The kernel polynomial method. *Rev. Mod. Phys.* **78**, 275–306 (2006).
67. Marzari, N., Mostofi, A. A., Yates, J. R., Souza, I. & Vanderbilt, D. Maximally localized Wannier functions: theory and applications. *Rev. Mod. Phys.* **84**, 1419–1475 (2012).

ACKNOWLEDGEMENTS

We thank I. Bloch, P.-Y. Chang, P. Coleman, B.J. DeSalvo, M. Foster, Y. Komijani, G. Pagano, A.M. Rey, M. Schütt, I. Spielman, and D. Vanderbilt for useful discussions. We also thank S. Gopalakrishnan and D. Huse for collaborations on related work and for insightful discussions. J.H.W. and J.H.P. acknowledge the Aspen Center for Physics where some of this work was performed, which is supported by National Science Foundation Grant No. PHY-1607611. J.H.P. is partially supported by the Air Force Office of Scientific Research under Grant No. FA9550-20-1-0136. E.J.K. was supported by the U.S. Department of Energy, Basic Energy Sciences, grant number DE-FG02-99ER45790. This work was supported by the Caltech Institute for Quantum Information and Matter, an NSF Physics Frontiers Center with support of the Gordon and Betty Moore Foundation and the Air Force Office for Scientific Research (J.H.W.). Y.-Z.C. was supported in part by a Simons Investigator award to Leo Radzihovsky and in part by the Army Research Office under Grant Number W911NF-17-1-0482.

The views and conclusions contained in this document are those of the authors and should not be interpreted as representing the official policies, either expressed or implied, of the Army Research Office or the U.S. Government. The U.S. Government is authorized to reproduce and distribute reprints for Government purposes notwithstanding any copyright notation herein. The authors acknowledge the Beowulf cluster at the Department of Physics and Astronomy of Rutgers University, The State University of New Jersey, and the Office of Advanced Research Computing (OARC) at Rutgers, The State University of New Jersey (http://oarc.rutgers.edu) for providing access to the Amarel cluster and associated research computing resources that have contributed to the results reported here.

AUTHOR CONTRIBUTIONS

E.J.K., J.H.W., and J.H.P. designed the research, Y.F., E.J.K., J.H.W., Y.-Z.C, and J.H.P. performed the research, and Y.F., E.J.K., J.H.W., Y.-Z.C., and J.H.P. wrote the paper.

COMPETING INTERESTS

The authors declare no competing interests.

ADDITIONAL INFORMATION

Supplementary information is available for this paper at https://doi.org/10.1038/s41535-020-00271-9.

Correspondence and requests for materials should be addressed to J.H.P.